Materials Science-Poland
Volume 43 Issue 4 · pp. 122–133 · DOI: 10.2478/msp-2025-0047

Materials Science-Poland

Enhancing the supercapacitor performance of MoS_2 nanostructures through metallic phase enrichment and morphology control

Research Article

Shrouq H. Aleithan[1]*, Sajid Ali Ansari[1], Shroq S. Laradhi[2], Khan Alam[3,4]

[1] *Department of Physics, College of Science, King Faisal University, P.O. Box 400, Al-Ahsa 31982, Kingdom of Saudi Arabia*
[2] *Department of Chemistry, College of Science, King Faisal University, P.O. Box 400, Al-Ahsa 31982, Kingdom of Saudi Arabia*
[3] *Department of Physics, College of Science, King Fahd University of Petroleum and Minerals, Dhahran 31261, Kingdom of Saudi Arabia*
[4] *Interdisciplinary Research Center for Renewable Energy and Power Systems, Dhahran, Saudi Arabia*

Received 21 October 2025; Accepted 30 December 2025

Abstract: Molybdenum disulfide (MoS_2) has attracted considerable attention as a promising electrode material for supercapacitor applications due to its tunable electronic structure and layered morphology. However, its electrochemical performance is highly dependent on the synthesis route and the resulting structural characteristics. In this study, MoS_2 nanostructures were synthesized using two distinct methods, hydrothermal synthesis (HT) and chemical vapor deposition (CVD), yielding materials with markedly different morphologies, particle sizes, and phase compositions. The HT method produced nanoscale MoS_2 with partial enrichment of the metallic 1T phase, while the CVD approach yielded highly crystalline, few-layer 2H-MoS_2 nanosheets. Electrodes were fabricated on nickel foam current collectors, whose three-dimensional porous architecture facilitated efficient charge transport and electrolyte accessibility. Electrochemical evaluation revealed that HT-MoS_2 exhibits superior supercapacitive performance, delivering a high specific capacitance of 466.66 F g^{-1} at a current density of 1 A g^{-1}, compared to 371.10 F g^{-1} for CVD-MoS_2. In addition, the HT-MoS_2 electrode demonstrated excellent galvanostatic charge–discharge behavior and retained high capacitance stability over 2,000 charge–discharge cycles. These results highlight the critical role of synthesis-driven phase and morphology engineering, as well as electrode architecture, in optimizing the supercapacitor performance of MoS_2-based materials and highlight their potential for advanced energy storage applications.

Keywords: *Supercapacitor • MoS_2 nanomaterials • CVD • Hydrothermal chemical method • Electrochemical performances • Charge storage*

1. Introduction

The rapid growth of renewable energy technologies has intensified the demand for efficient, durable, and environmentally sustainable energy storage systems. Among electrochemical energy storage devices, supercapacitors have attracted significant attention due to their high power density, fast charge–discharge capability, and long cycle life, making them suitable for applications ranging from portable electronics to hybrid energy systems. Supercapacitors are generally classified into electric double-layer capacitors (EDLCs), which store charge through electrostatic ion adsorption, and pseudocapacitors, which rely on fast and reversible Faradaic redox reactions [1,2]. While EDLCs exhibit excellent cycling stability, their relatively low energy density limits broader applications, thereby motivating the development of advanced pseudocapacitive electrode materials.

The performance of supercapacitor electrodes is strongly governed by the physicochemical properties of the active materials, including electrical conductivity, accessible surface area, ion diffusion pathways, and the density of electrochemically active sites. Carbon-based materials are widely used in EDLCs [3,4]; however, their limited specific capacitance has prompted increasing interest in pseudocapacitive materials such as transition

* *E-mail: salaithan@kfu.edu.sa*

metal oxides, hydroxides, sulfides, and conducting polymers [3,5]. In this context, layered transition metal dichalcogenides (TMDs) have emerged as promising candidates owing to their two-dimensional crystal structure, tunable electronic properties, and abundance of exposed edge sites that facilitate redox reactions. Molybdenum disulfide (MoS_2) is among the most extensively investigated TMDs for energy storage applications due to its layered structure, mechanical flexibility, chemical stability, and multiple oxidation states of molybdenum [4,6]. MoS_2 exists primarily in two crystallographic phases: the thermodynamically stable semiconducting 2H phase and the metastable metallic 1T phase. These phases exhibit markedly different electrical conductivities and electrochemical behaviors. The 2H phase generally suffers from limited electrical conductivity, whereas the metallic 1T phase offers enhanced charge transport and faster redox kinetics, which are highly desirable for supercapacitor electrodes. For example, hydrothermally prepared 2H-MoS_2 nanoflowers provide a specific capacitance of 255.65 F g^{-1} at 0.25 A g^{-1} [7], while 1T-MoS_2 microspheres yield 228 F g^{-1} [8]. Interestingly, materials containing both phases display exceptional performance, with specific capacitance values as high as 742 F g^{-1} [9]. Consequently, strategies aimed at phase engineering and morphology control have been widely explored to improve the electrochemical performance of MoS_2-based materials.

Structural modification through doping has also proven effective; for instance, Ni-doped MoS_2 on carbon cloth electrodes achieves 305.9 F g^{-1}, compared to 170.2 F g^{-1} for pristine MoS_2 [10]. Another strategy to enhance the conductivity of MoS_2 involves the incorporation of carbon-based composites. For example, MoS_2 nanobelts/carbon hybrids exhibit 77.5 F g^{-1} at 0.5 A g^{-1} [11], while carbon nanotube/MoS_2 composites reach 150 F g^{-1} at 0.2 A g^{-1} [12]. Mixed-phase MoS_2 nanoflakes/carbon nanofiber composites show a remarkable specific capacitance of 626.08 F g^{-1} at 1 A g^{-1}, compared to only 159.35 F g for pristine MoS_2 [13].

Previous studies have demonstrated that the synthesis method plays a decisive role in determining the phase composition, morphology, and electrochemical properties of MoS_2. Hydrothermal synthesis often yields nanostructured MoS_2 with reduced particle size, abundant defects, and partial transformation from the 2H to the metallic 1T phase, leading to improved pseudocapacitive performance. In contrast, chemical vapor deposition (CVD) typically produces highly crystalline, large-area MoS_2 nanosheets dominated by the 2H phase, which are advantageous for electronic and optoelectronic applications but may exhibit limited capacitance due to a lower density of active sites and reduced ionic accessibility. Despite extensive studies on MoS_2-based supercapacitor electrodes, a direct and systematic comparison between MoS_2 synthesized by fundamentally different routes, namely, CVD and hydrothermal methods, remains relatively unexplored. Such a comparison is crucial for establishing clear correlations between synthesis strategy, structural features, phase composition, and electrochemical performance. Understanding these relationships is essential for rational electrode design and for selecting appropriate synthesis routes tailored to high-performance energy storage applications.

In this work, we present a comparative study of MoS_2 nanostructures synthesized via CVD and a hydrothermal (HT) method employing a polymeric surfactant additive. The CVD approach yields few-layer, highly crystalline MoS_2 nanosheets, whereas the hydrothermal route produces nanospherical MoS_2 with reduced particle size and a mixed 1T/2H phase composition. Comprehensive structural and morphological characterization was carried out using X-ray diffraction (XRD), Raman spectroscopy, Fourier-transform infrared spectroscopy (FTIR), scanning electron microscopy (SEM), and transmission electron microscopy (TEM). The supercapacitive performance of both materials was systematically evaluated using cyclic voltammetry (CV), galvanostatic charge–discharge measurements, and cycling stability tests. The results demonstrate that hydrothermally synthesized MoS_2 exhibits superior electrochemical performance, which is attributed to the synergistic effects of metallic phase enrichment and nanoscale morphology. This study provides valuable insights into the role of synthesis-driven phase and morphology control in optimizing MoS_2-based electrodes for next-generation supercapacitor applications.

2. Materials

Ammonium molybdate tetrahydrate ($(NH_4)_6Mo_7O_{24}{\cdot}4H_2O$) and thioacetamide ($CH_3CSNH_2$, ≥99.0%) were purchased from Sigma-Aldrich and used as molybdenum and sulfur precursors, respectively. Tergitol NP-9, a nonionic surfactant, was also obtained from Sigma-Aldrich and used as a morphology- and phase-regulating agent during hydrothermal synthesis. Molybdenum trioxide (MoO_3, 99.5%) was supplied by Alfa Aesar, and sulfur powder (99.9%) was purchased from VWR Chemicals. All reagents were used without further purification, and deionized water was employed throughout the experiments.

3. Hydrothermal synthesis of MoS_2 nanostructures (HT-MoS_2)

HT-MoS_2 was synthesized via a hydrothermal chemical route. In a typical synthesis, 1.41 g of ammonium molybdate tetrahydrate and 0.26 g of thioacetamide were dissolved in 20 mL of deionized water under continuous magnetic stirring to obtain a clear and homogeneous solution. Subsequently, 36 µL of Tergitol NP-9 was added, and the mixture was stirred for an additional 30 min to ensure uniform dispersion of the surfactant molecules. The homogeneous solution was transferred into a 100 mL Teflon-lined stainless-steel autoclave, sealed, and maintained at 200°C for 24 h without a controlled heating rate. Upon completion of the reaction, the autoclave was allowed to cool naturally to room temperature. The resulting black precipitate was collected by centrifugation and washed several times with deionized water and ethanol to remove unreacted species and residual surfactant. The final product was dried at 60°C, yielding HT-MoS_2 powder enriched in the metallic phase [14]. The addition of Tergitol NP-9 plays a critical role in controlling particle growth and morphology during hydrothermal synthesis. The surfactant induces lattice distortion and structural strain, which promotes partial phase transformation from the semiconducting 2H phase to the metallic 1T phase while simultaneously stabilizing the metastable 1T structure. This results in nanosized MoS_2 particles with enhanced electrochemical activity.

4. Chemical vapor deposition of MoS_2 nanosheets (CVD-MoS_2)

CVD-MoS_2 nanosheets were synthesized using a horizontal quartz-tube chemical vapor deposition system. A mixture of MoO_3 and NaCl (40 wt%) was placed in a quartz boat at the center of the furnace, serving as the molybdenum source. A clean quartz substrate was positioned downstream to collect the grown MoS_2 film. Prior to deposition, the substrate was sequentially cleaned with acetone and methanol, followed by sonication in deionized water and drying under nitrogen flow. The furnace temperature was ramped to 780°C at a heating rate of 20°C min^{-1} under a constant nitrogen flow of 20 sccm. Sulfur powder (200 mg), placed outside the main heating zone, was heated separately to 250°C using an external heater once the furnace reached the target temperature. The sulfur vapor was transported into the reaction zone by the carrier gas, and the growth was maintained for 20 min. After synthesis, the furnace was allowed to cool naturally to room temperature under a nitrogen atmosphere.

The synthesis procedure followed the method reported by Aleithan et al. [15], in which NaCl was employed as a growth promoter to reduce the effective melting point of MoO_3. The as-grown MoS_2 film was mechanically scraped from the substrate, dispersed in deionized water, and sonicated for 3 h to obtain CVD-MoS_2 powder for electrochemical studies.

5. Structural and morphological characterization

Phase composition and crystallinity were examined using XRD with Cu Kα radiation (λ = 0.154 nm) (Malvern, GH Eindhoven, Netherlands). Raman spectroscopy (HORIBA, LabRAM HR, excitation wavelength 445 nm) was employed to identify vibrational modes associated with the 2H and 1T phases of MoS_2. FTIR spectroscopy was used to investigate chemical bonding and functional groups using a Bruker spectrometer (Ettlingen 76275, Germany). Surface morphology and elemental composition were analyzed using SEM equipped with energy-dispersive X-ray spectroscopy (EDX) (Tescan Vega 3 SBU, Czech Republic). High-resolution transmission electron microscopy (HRTEM) and selected area electron diffraction (SAED) (JEOL JEM-2100, Tokyo, Japan) were used to determine particle size, interlayer spacing, and crystallographic features.

6. Electrode fabrication and electrochemical measurements

Electrochemical performance was evaluated using a three-electrode configuration with a potentiostat/galvanostat. The working electrodes were prepared by mixing 80 wt% active material (HT-MoS_2 or CVD-MoS_2), 10 wt% carbon black, and 10 wt% polytetrafluoroethylene (PTFE) binder to form a uniform slurry, following our previously reported method [16]. The slurry was coated onto nickel foam substrates (1 × 1 cm^2), which served as conductive current collectors due to their high electrical conductivity and porous three-dimensional structure. The mass loading of active material was approximately 1 mg for all electrodes. The coated electrodes were dried at 60°C before electrochemical testing.

Electrochemical measurements were performed in 2 M KOH aqueous electrolyte using an Ag/AgCl reference electrode and a platinum plate counter electrode. CV and

galvanostatic charge–discharge (GCD) tests were conducted within a potential window of 0.0–0.45 V (Nova Auto Lab, Metrohm). The specific capacitance (C, F g^{-1}) was calculated from GCD curves according to the following equations:

$$C = \frac{I\Delta t}{m\Delta V}$$

where I is the discharge current, Δt is the discharge time, m is the mass of the active material, and ΔV is the potential window.

To ensure a fair comparison, all capacitance values were normalized to the mass of the active material. The nickel foam substrate was used solely as a current collector, and its contribution to the measured capacitance was consistent for both electrodes.

7. Results and discussion

7.1 Structural and phase analysis

Figure 1(a) shows the XRD pattern of the CVD-grown MoS_2 sample. The sharp and well-defined diffraction peaks indicate high crystallinity and the formation of few-layer MoS_2 nanosheets. All major diffraction peaks can be indexed to the hexagonal 2H-MoS_2 phase (JCPDS No. 75-1539), confirming that the CVD process predominantly yields the thermodynamically stable semiconducting phase [17]. The intense (002) diffraction peak observed at $2\theta \approx 14.68°$ corresponds to an interlayer spacing (d) of 0.61 nm, which is the characteristic of few-layer MoS_2. The corresponding lattice parameter along the c-axis was calculated as $c = 2d = 1.22$ nm. The lattice parameter a was determined from the (104) reflection at $2\theta = 44.53°$, yielding a value of 0.316 nm. These lattice parameters are in excellent agreement with standard values reported for hexagonal 2H-MoS_2 with space group $P6_3/mmc$, confirming the high crystallinity and phase purity of the CVD-grown sample.

Minor diffraction peaks observed near 23° and 30° are attributed to residual MoO_3 (JCPDS No. 05-0508), while the weak peak around 28° is likely associated with trace quartz fragments introduced during mechanical removal of the film from the substrate. The MoO_3 content was estimated to be approximately 12.5% using the reference intensity ratio method, based on the intensity ratio of the MoO_3 (110) peak to the MoS_2 (002) peak.

Figure 1(b) shows the XRD pattern of the hydrothermally synthesized MoS_2 (HT-MoS_2). The diffraction peaks are significantly broadened compared to the CVD-grown sample, indicating reduced crystallite size, lattice distortion, and partial amorphization associated with nanoscale materials. The (002) reflection is shifted to a lower diffraction angle of approximately $2\theta \approx 12.5°$, corresponding to an expanded interlayer spacing of $d \approx 0.707$ nm and a lattice parameter of $c \approx 1.414$ nm. Such interlayer expansion is characteristic of structural strain and is commonly associated with partial phase transformation from the hexagonal 2H phase to the metallic 1T phase, which possesses a

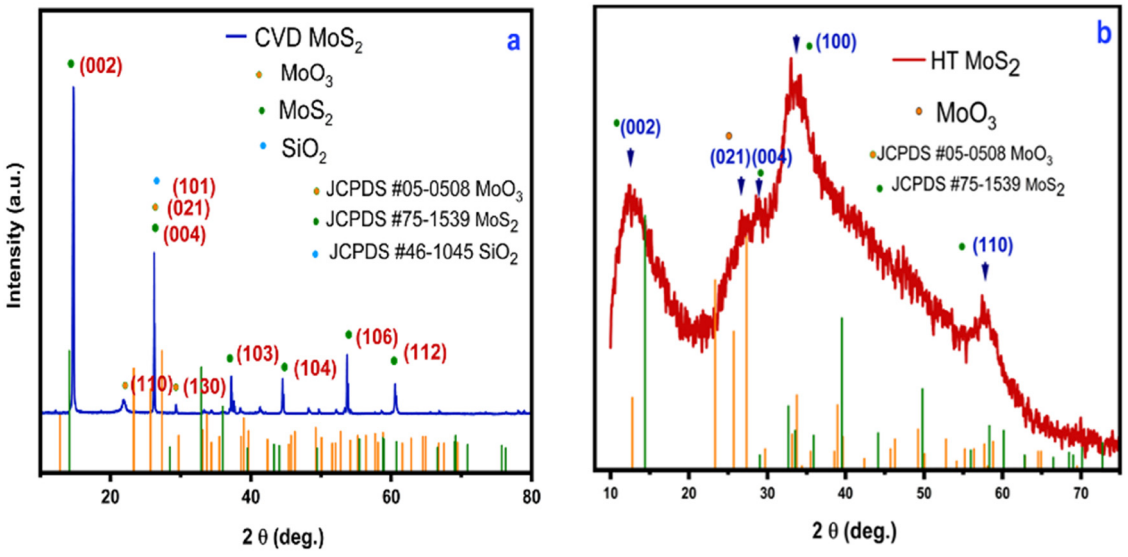

Figure 1. XRD patterns for (a) CVD MoS_2 and (b) HT MoS_2.

distorted octahedral coordination of Mo atoms [18]. The lattice parameter a, estimated from the broad (100) reflection centered near $2\theta \approx 33°$, was calculated to be approximately 0.313 nm, a value close to those reported for both hexagonal 2H and octahedral 1T MoS_2, supporting the coexistence of semiconducting and semimetallic phases in the HT-MoS_2 sample. Additional weak and broad features observed in Figure 1(b) may originate from residual MoO_3, consistent with the Raman and FTIR analyses. The presence of the distorted octahedral 1T phase, together with expanded interlayer spacing and nanoscale crystallite size, is expected to enhance electrical conductivity, increase the density of electrochemically active sites, and facilitate ion transport, thereby directly contributing to the improved supercapacitive performance of the HT-MoS_2 electrode.

8. Raman spectroscopy and semi-quantitative phase analysis

Raman spectroscopy was employed to further investigate the phase composition and structural disorder of the samples. As shown in Figure 2(a), the CVD-MoS_2 sample exhibits two prominent Raman-active modes at approximately 385 cm^{-1} (E_{2g}, in-plane vibration) and 405 cm^{-1} (A_{1g}, out-of-plane vibration). The separation between these modes of about 20 cm^{-1} is indicative of few-layer MoS_2 with high crystallinity and confirms the dominance of the 2H phase [19,20]. Weak and broadened Raman features associated with MoO_3 indicate its low concentration and poor crystallinity, in good agreement with the XRD results. No Raman signatures of quartz are observed, suggesting that quartz is not uniformly distributed within the sample and is more likely present as isolated fragments introduced during mechanical removal of the film from the substrate.

In contrast, the Raman spectrum of HT-MoS_2 (Figure 2(b)) shows broadened and weakened E_{2g} (376.5 cm^{-1}) and A_{1g} modes, reflecting reduced crystallinity and increased structural disorder. Notably, additional peaks appear at approximately 145, 238, and 336 cm^{-1}, corresponding to the J_1, J_2, and J_3 vibrational modes, which are characteristic fingerprints of the metallic 1T-MoS_2 phase [21–24]. A semi-quantitative assessment of the phase composition was performed by comparing the relative intensity of the J modes to that of the E_{2g} mode. The pronounced intensity of the J_1–J_3 bands in HT-MoS_2 indicates significant enrichment of the metallic 1T phase compared to the purely 2H-dominated CVD-MoS_2 sample. The Raman-based 1T/2H intensity ratio exceeds 1, indicating dominant 1T spectral contributions when considering relative intensity ratios rather than absolute phase fractions.

Although precise quantification requires X-ray photoelectron spectroscopy, the Raman analysis provides reliable evidence of phase transformation induced by the hydrothermal synthesis route. Moreover, sharp Raman peaks at 111, 123, 194.3, and 220 cm^{-1} are attributed to crystalline MoO_3 nanoparticles, as shown in Figure 2(b) and consistent with previous reports [23,25,26]. Combined Raman and XRD analyses confirm that both samples predominantly consist of hexagonal 2H-MoS_2 with minor MoO_3 impurities [27]. In contrast, the HT-MoS_2 sample additionally exhibits a pronounced partial phase transformation from semiconducting

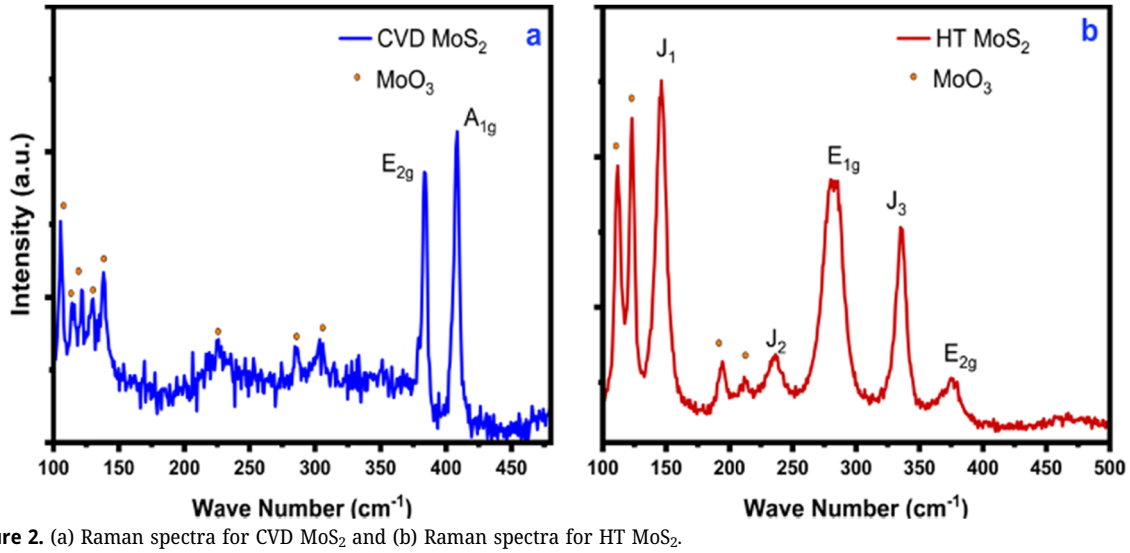

Figure 2. (a) Raman spectra for CVD MoS_2 and (b) Raman spectra for HT MoS_2.

2H-MoS_2 to metallic 1T-MoS_2, consistent with the observed J-mode features and structural distortions.

The FTIR spectra of both samples (Figure 3(a) and (b)) exhibit characteristic absorption bands corresponding to Mo–S bonding, confirming the formation of MoS_2. The band near 1,400 cm^{-1} is attributed to S–Mo–S stretching vibrations, while peaks in the range of 590–620 cm^{-1} correspond to Mo–S stretching modes. Additional bands observed between 860 and 1,100 cm^{-1} are assigned to Mo–O and O–Mo–O vibrations, indicating the presence of minor MoO_3 species. Broad absorption features around 1,600 and 3,000 cm^{-1} arise from hydroxyl groups associated with adsorbed moisture or surface-bound species.

9. Morphological analysis

SEM images of CVD-MoS_2 (Figure 4(a) and (b)) reveal large-area, layered flakes with lateral dimensions exceeding 5 μm, consistent with the high crystallinity observed in XRD and Raman analyses. The smooth and continuous morphology suggests limited edge exposure and reduced ion-accessible surface area, which may restrict electrochemical activity despite excellent structural quality.

In contrast, HT-MoS_2 exhibits a nanoparticulate morphology, as shown in Figure 4(c) and (d). The particles are uniformly distributed and form loosely agglomerated nanospheres with sizes below 100 nm. TEM analysis (Figure 5) reveals that the HT-MoS_2 nanoparticles have an average diameter of approximately 50 nm and possess sharp edges and multigrain structures. The expanded interlayer spacing observed in HRTEM images (~0.75 nm) further confirms the presence of the metallic 1T phase and structural strain. The SAED pattern exhibits continuous diffraction rings (Figure 5(e)), confirming the polycrystalline nature of the HT-MoS_2 nanocrystals. Such nanoscale features significantly increase the accessible surface area and provide abundant electrochemically active edge sites. The EDX spectra confirm the presence of Mo, S, and O in both samples; however, precise quantitative determination of their weight ratios is limited due to overlap between the S Kα (2.31 keV) and Mo Lα (2.29 keV) emission lines (Figure 4(e) and (f)). The detected oxygen signal further supports the presence of minor MoO_3 species, consistent with the XRD and Raman analyses.

10. Electrochemical performances

The electrochemical performance of HT-MoS_2 and CVD-MoS_2 electrodes was evaluated using CV and GCD measurements in a three-electrode configuration with 2 M KOH electrolyte. Figure 6(a) shows the CV curves recorded at a scan rate of 30 mV s^{-1}. Both electrodes exhibit distinct redox peaks, indicating pseudocapacitive behavior governed by reversible Faradaic reactions. Notably, the CV curve of HT-MoS_2 encloses a significantly larger area than that of CVD-MoS_2, reflecting its higher charge-storage capability. CV measurements performed at various scan rates (Figure 7(a) and (b)) demonstrate that HT-MoS_2 maintains well-defined redox features even at higher scan rates, indicating improved charge-transfer kinetics and

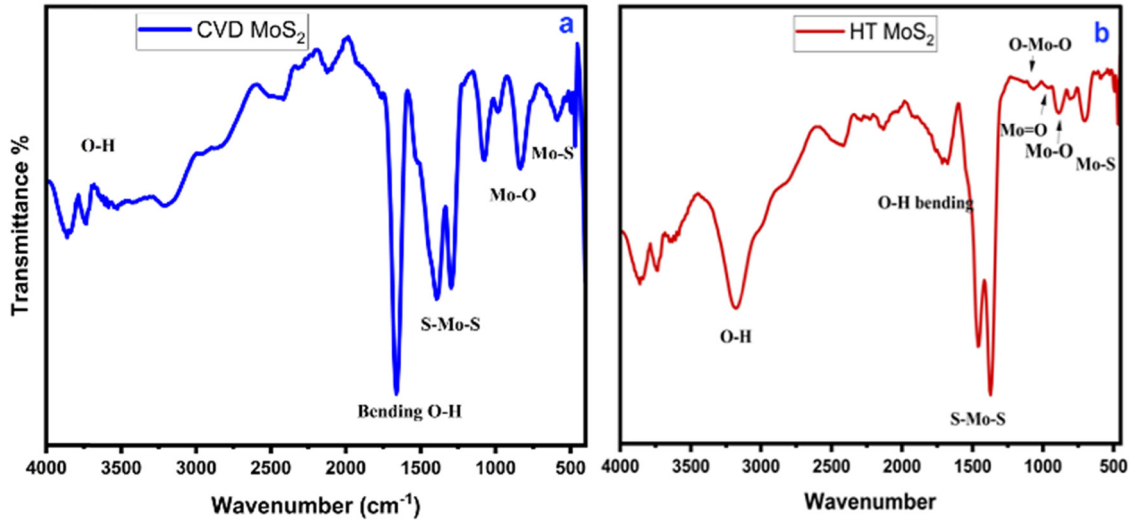

Figure 3. (a) FTIR spectra for CVD MoS_2 and (b) FTIR spectra for HT MoS_2.

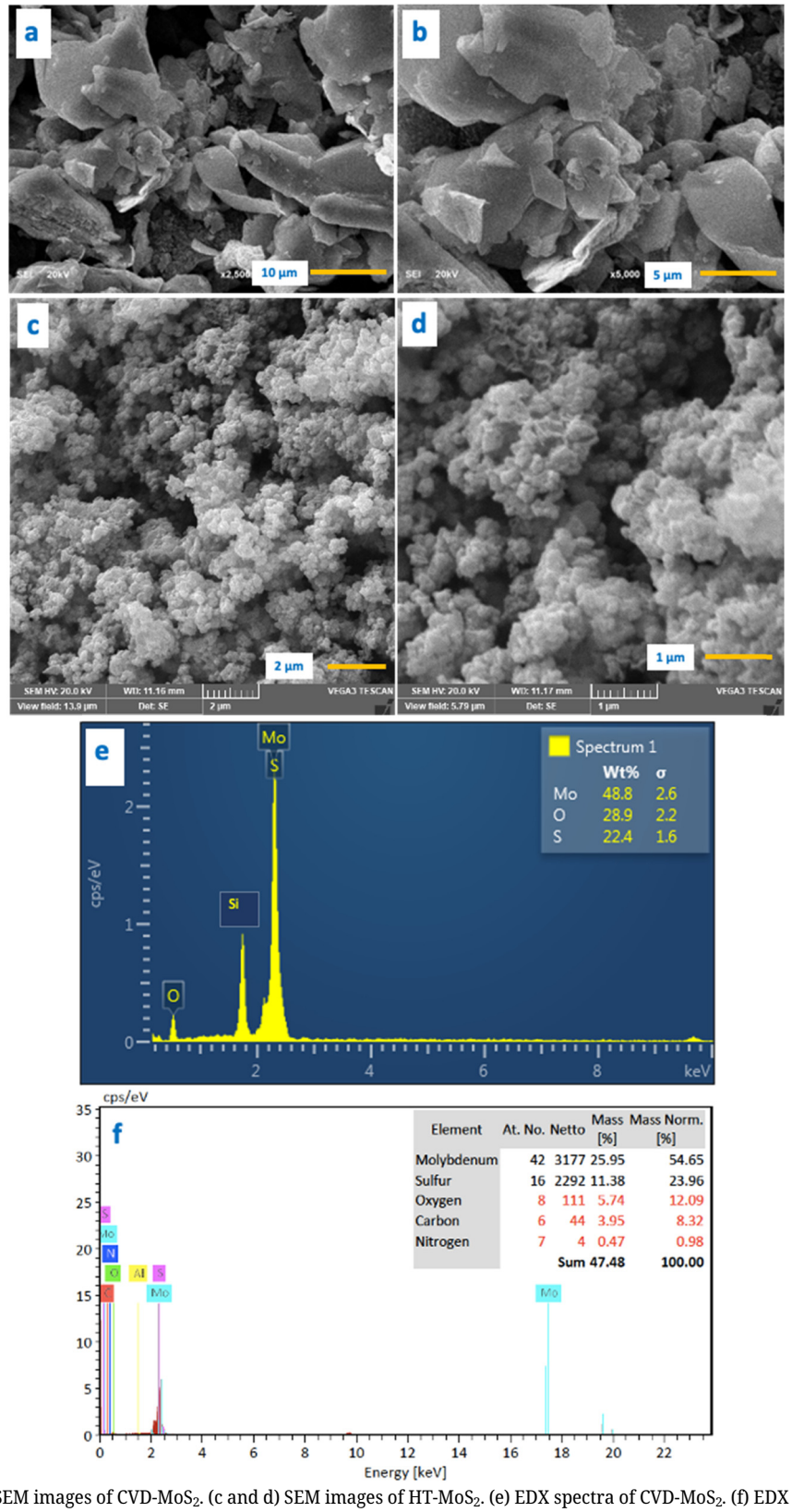

Figure 4. (a and b) SEM images of CVD-MoS_2. (c and d) SEM images of HT-MoS_2. (e) EDX spectra of CVD-MoS_2. (f) EDX spectra of HT-MoS_2.

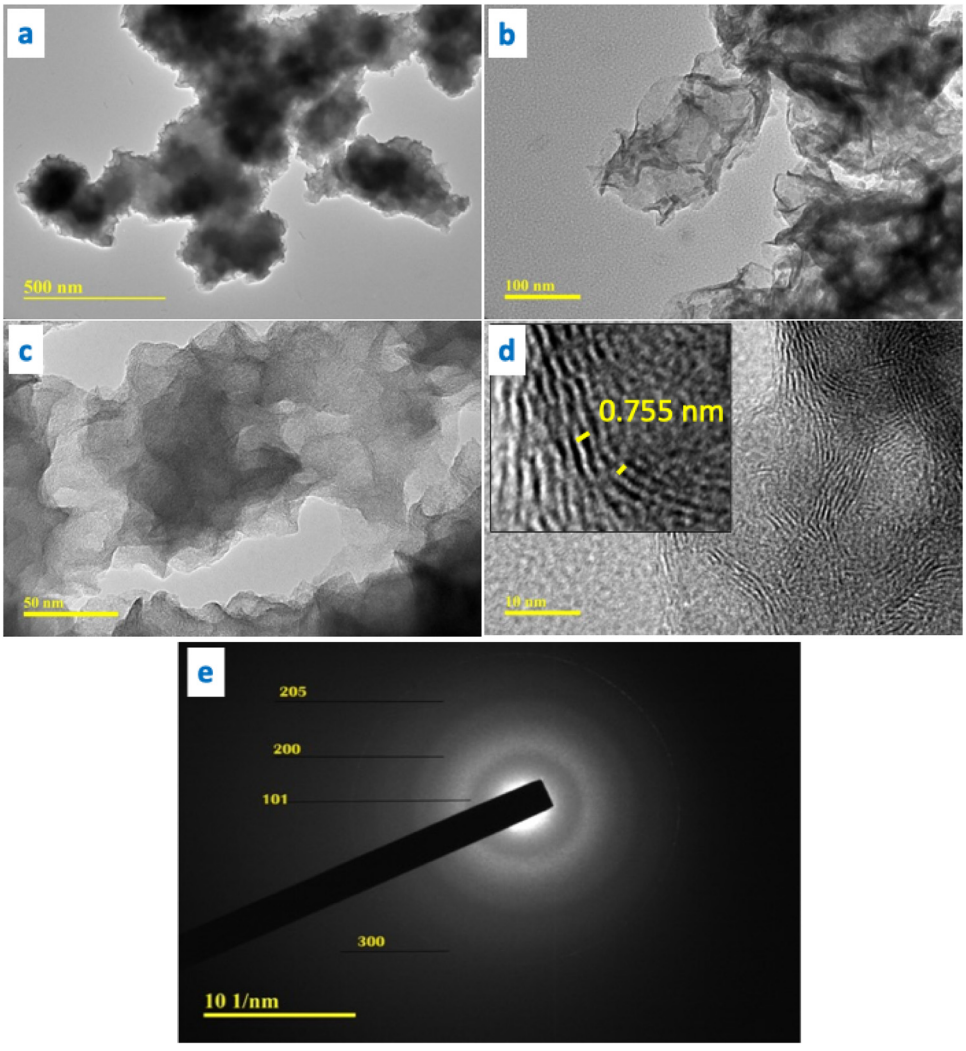

Figure 5. (a–c) Different magnification HRTEM images for the HT MoS_2 sample. (d) HRTEM shows layer structures with an average layer interspacing of 0.755 nm. (e) SAED pattern for the HT-MoS_2 sample.

ion diffusion. This enhanced performance is attributed to the metallic 1T phase, which provides higher electrical conductivity, and the nanoscale morphology, which shortens ion diffusion pathways.

GCD curves recorded at a current density of 1 A g^{-1} (Figure 7(c) and (d)) further confirm the superior performance of HT-MoS_2. The specific capacitance of HT-MoS_2 reaches 466.66 F g^{-1}, significantly higher than the 371.10 F g^{-1} obtained for CVD-MoS_2. At increasing current densities, HT-MoS_2 consistently outperforms CVD-MoS_2, demonstrating superior rate capability. The HT-MoS_2 electrode delivered specific capacitance values of 466.66, 444.40, 432.50, 280.00, 176.00, 113.50, and 89.00 F g^{-1} at 1, 1.25, 1.5, 1.75, 2, 3, and 5 A g^{-1}, respectively. By contrast, the CVD-MoS_2 electrode exhibited capacitances of 371.10, 269.50, 156.60, 81.70, 75.55, 53.40, and 44.10 F g^{-1} at the same current densities. This behavior highlights the synergistic effect of metallic phase enrichment and nanoscale morphology on electrochemical performance.

11. Cycling stability and electrode considerations

The long-term cycling stability of the HT-MoS_2 electrode was evaluated over 2,000 charge–discharge cycles (Figure 8). The electrode retained approximately 89.23% of its initial capacitance, indicating excellent structural and electrochemical stability. The robust cycling performance can be

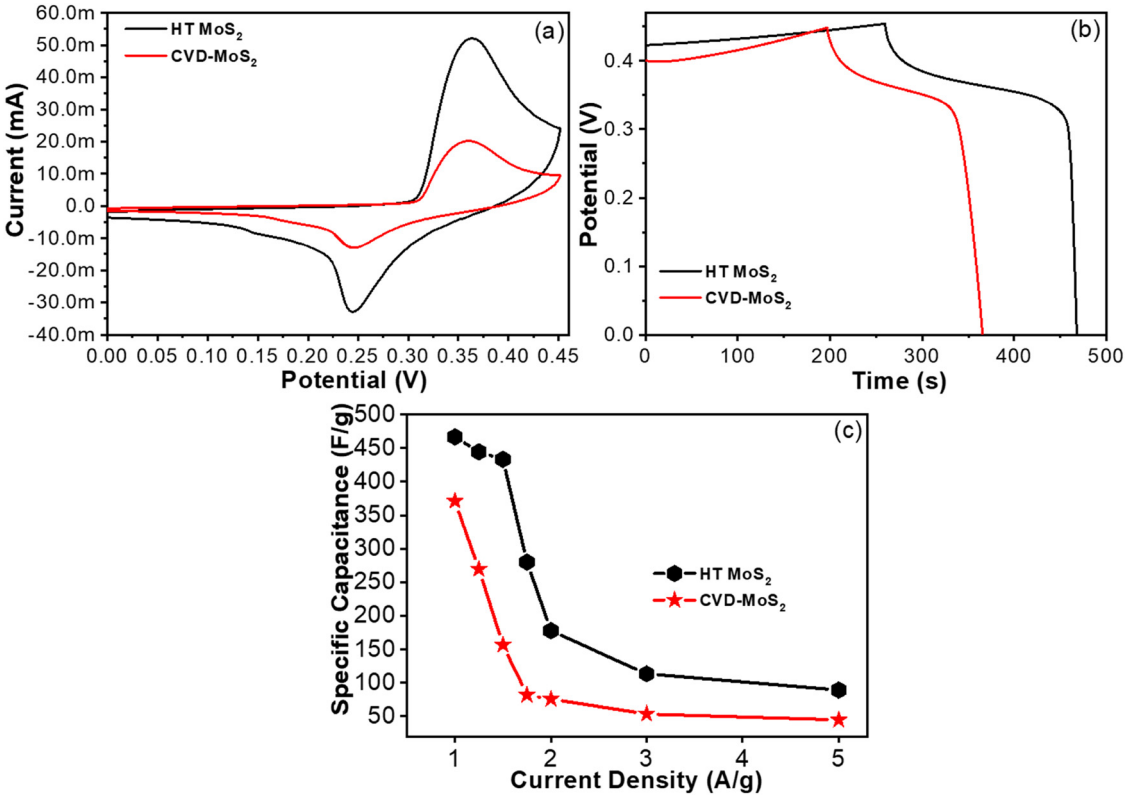

Figure 6. Comparative (a) CV, (b) CD, and (c) calculated specific capacitance of the HT-MoS_2 and CVD-MoS_2 electrodes at fixed current loads.

attributed to the stable coexistence of 1T and 2H phases and the mechanically resilient nanostructure. It is important to note that nickel foam was employed solely as a conductive current collector due to its three-dimensional porous structure. All capacitance values were normalized to the mass of the active material, and identical substrates and mass loadings were used for both electrodes. Therefore, the observed differences in electrochemical performance primarily reflect the intrinsic properties of the synthesized MoS_2 materials rather than contributions from the substrate.

While the 1T phase enhances electrical conductivity and charge transfer, the amorphous domains introduce structural disorder, provide abundant active sites, and facilitate ion diffusion. Together, these features are responsible for the remarkable capacitance and cycling stability observed.

The comparative analysis clearly demonstrates that the hydrothermal synthesis route is more effective than CVD for producing MoS_2 with enhanced supercapacitive performance. While CVD yields highly crystalline, large-area nanosheets dominated by the 2H phase, the hydrothermal method enables phase engineering and morphology control, resulting in metallic phase enrichment and nanoscale particles with abundant active sites. These structural advantages translate directly into higher specific capacitance, improved rate capability, and excellent cycling stability, highlighting the critical role of synthesis-driven phase and morphology optimization in MoS_2-based supercapacitor electrodes.

These results surpass those reported in recent studies on MoS_2 nanostructures modified via plasma treatment or heteroatom doping to enhance electrical conductivity and defect density for energy storage applications [28–30].

The enrichment of the metallic 1T phase in HT-MoS_2 plays a critical role in enhancing electrochemical performance. The distorted octahedral coordination of Mo atoms in the 1T phase results in a higher electronic density of states at the Fermi level, leading to improved electrical conductivity compared to the semiconducting 2H phase. In addition, the structural disorder and reduced crystallite size associated with the hydrothermal synthesis introduce a higher density of edge sites and defects, which serve as electrochemically active centers for Faradaic charge storage. These combined effects facilitate faster charge transfer and ion diffusion during electrochemical cycling, consistent with the superior capacitance and rate capability observed for the HT-MoS_2 electrode [31–34].

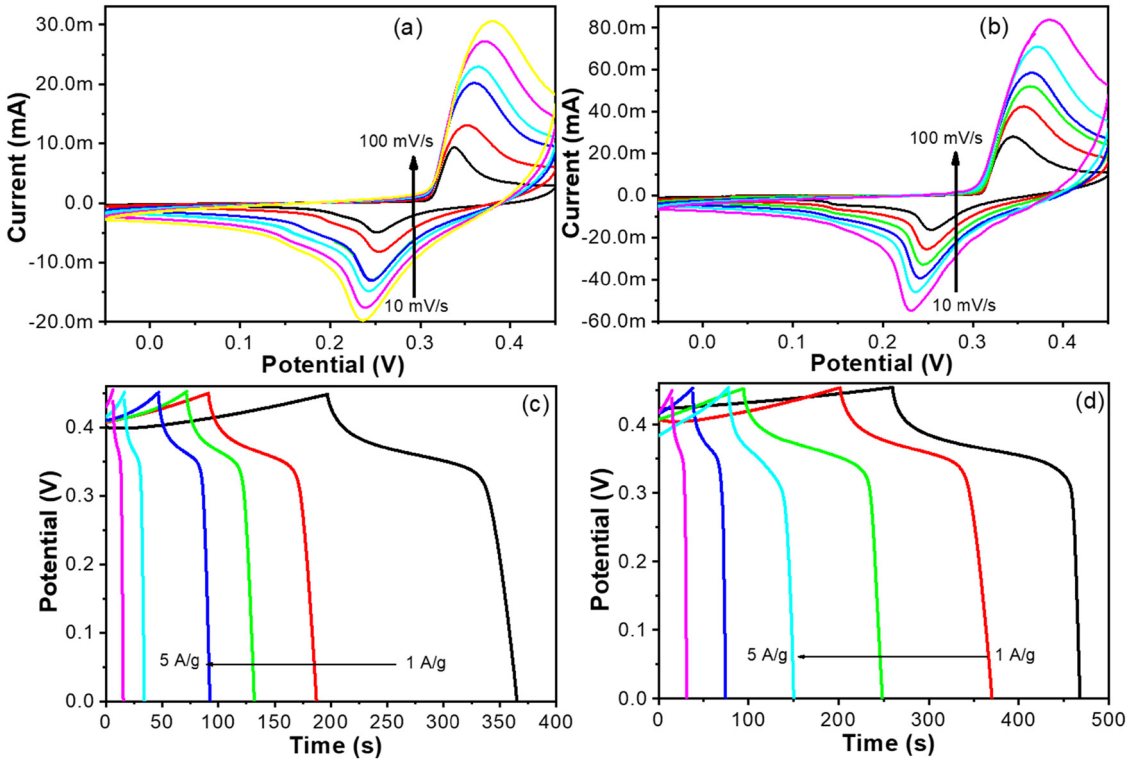

Figure 7. CV profile of the (a) CVD-MoS_2 and (b) HT-MoS_2, and GCD profile of the (c) CVD-MoS_2 and (d) HT-MoS_2 electrodes.

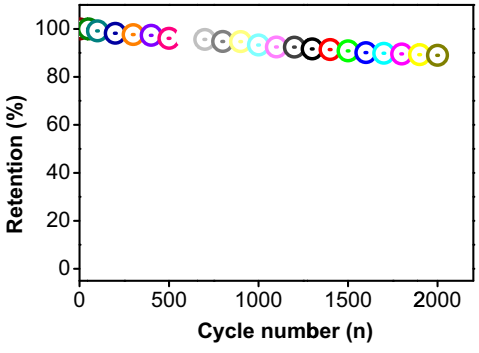

Figure 8. Percent retention profile of the HT-MoS_2 electrode.

12. Conclusions

In this work, MoS_2 nanostructures were synthesized via CVD and a hydrothermal (HT) method to elucidate the influence of synthesis strategy on phase composition, morphology, and supercapacitor performance. The CVD-grown MoS_2 consisted of highly crystalline, few-layer nanosheets dominated by the semiconducting 2H phase, whereas the hydrothermal route produced nanoscale MoS_2 particles with expanded interlayer spacing and significant enrichment of the metallic 1T phase. Structural and spectroscopic analyses confirmed the coexistence of 1T and 2H phases in HT-MoS_2, accompanied by reduced crystallite size and increased defect density.

Electrochemical measurements revealed that HT-MoS_2 exhibits superior specific capacitance, enhanced rate capability, and excellent cycling stability compared to its CVD counterpart. These improvements are attributed to the synergistic effects of metallic phase enrichment, nanoscale morphology, and increased density of electrochemically active sites, which collectively enhance electrical conductivity and ion transport kinetics. This study highlights the critical role of synthesis-driven phase and morphology engineering in optimizing MoS_2-based electrode materials and provides valuable insights for the rational design of high-performance supercapacitors.

Acknowledgments

This work was supported by the Annual Funding track by the Deanship of Scientific Research, Vice Presidency for Graduate Studies and Scientific Research, King Faisal University, Saudi Arabia [Project No. KFU252468].

Author contributions

Shrouq Aleithan: investigation, funding acquisition; Shroq Laradhi and Shrouq Aleithan: sample preparation; Shrouq Aleithan, Sajid Ansari and Khan Alam: characterization, data curation, and formal analysis; Shrouq Aleithan and Sajid Ansari: writing – original draft, review & editing.

Conflict of interest statement

Authors state no conflict of interest.

References

[1] Karthikeyan, S., Narenthiran, B., Sivanantham, A., Bhatlu, L.D., Maridurai T., Supercapacitor: evolution and review, Mater. Today Proc., 2021, 46: 3984–3988. doi: 10.1016/j.matpr.2021.02.526

[2] Şahin, M.E., Blaabjerg, F., Sangwongwanich, A., A comprehensive review on supercapacitor applications and developments, Energies, 2022, 15(3): 674. doi: 10.3390/en15030674

[3] Bello, I.T., Oladipo, A.O., Adedokun, O., Dhlamini, S.M., Recent advances on the preparation and electrochemical analysis of MoS_2-based materials for supercapacitor applications: a mini-review, Mater. Today Commun., 2020, 25: 101664. doi: 10.1016/j.mtcomm.2020.101664

[4] Mohan, M., Shetti, N.P., Aminabhavi, T.M., Phase dependent performance of MoS_2 for supercapacitor applications, J. Energy Storage, 2023, 58: 106321. doi: 10.1016/j.est.2022.106321

[5] Mohan, M., Shetti, N.P., Aminabhavi, T.M., Recent developments in MoS_2-based flexible supercapacitors, Mater. Today Chem., 2023, 27: 101333. doi: 10.1016/j.mtchem.2022.101333

[6] Joseph, N., Shafi, P.M., Bose, A.C., Recent advances in 2D-MoS_2 and its composite nanostructures for supercapacitor electrode application, Energy Fuels, 2020, 34(6): 6558–6597. doi: 10.1021/acs.energyfuels.0c00430

[7] Gupta, H., Chakrabarti, S., Mothkuri, S., Padya, B., Rao, T.N., Jain, P.K., High performance supercapacitor based on 2D-MoS_2 nanostructures, Mater. Today Proc., 2020, 26: 20–24. doi: 10.1016/j.matpr.2019.04.198

[8] Sun, X., Pang, Y., Li, S., Yu, Y., Ding, X., Wang, L., et al., High performance asymmetric supercapacitor based on 3D microsphere-like 1T-MoS_2 with high 1T phase content, Ceram. Int. 2022, 48(15): 21317–21326. doi: 10.1016/j.ceramint.2022.04.098

[9] Kour, P., Deeksha, Yadav, K., Electrochemical performance of mixed-phase 1T/2H MoS_2 synthesized by conventional hydrothermal v/s microwave-assisted hydrothermal method for supercapacitor applications, J. Alloys Compd., 2022, 922: 166194. doi: 10.1016/j.jallcom.2022.166194

[10] Saseendran, S.B., Ashok, A., Asha, A.S., Flexible and binder-free supercapacitor electrode with high mass loading using transition metal doped MoS_2 nanostructures, J. Alloys Compd., 2023, 968: 172131. doi: 10.1016/j.jallcom.2023.172131

[11] Khandare, L.N., Late, D.J., Chaure, N.B., MoS_2 nanobelts–carbon hybrid material for supercapacitor applications, Front. Chem., 2023, 11: 1166544. doi: 10.3389/fchem.2023.1166544

[12] Tobis, M., Sroka, S., Frąckowiak, E., Supercapacitor with carbon/MoS_2 composites, Front. Energy Res., 2021, 9: 647878

[13] Kour, P., Deeksha, Kour, S., Sharma, A.L., Yadav, K., Mixed-phase MoS_2 nanosheets anchored carbon nanofibers for high energy symmetric supercapacitors, J. Energy Storage, 2023, 63: 107054. doi: 10.1016/j.est.2023.107054

[14] Venkateshwaran, S., Senthil Kumar, S.M., Template-driven phase selective formation of metallic 1T-MoS_2 nanoflowers for hydrogen evolution reaction, ACS Sustain. Chem. Eng., 2019, 7(2): 2008–2017. doi: 10.1021/acssuschemeng.8b04335

[15] Aleithan, S.H., Al-Amer, K., Alhashem, Z., Alati, N.A., Alabbad, Z.H., Alam, K., Growth of MoS_2 films: high-quality monolayered and multilayered material, AIP Adv., 2022, 12(7): 075220, doi: 10.1063/5.0086228

[16] Aleithan, S.H., Ansari, S.A., Perdana, M.Y., Alam, K., Alhashem, Z., Al-Amer, K., The controllable ratio of the polyaniline-needle-shaped manganese dioxide for the high-performance supercapacitor application, Nanomaterials, 2023, 13(1): 101. doi: 10.3390/nano13010101

[17] Ardahe, M., Hantehzadeh, M.R., Ghoranneviss, M., Effect of growth temperature on physical properties of MoS_2 thin films synthesized by CVD, J. Electron. Mater., 2020, 49(2): 1002–1008. doi: 10.1007/s11664-019-07796-1

[18] Rasamani, K.D., Alimohammadi, F., Sun, Y., Interlayer-expanded MoS_2, Mater. Today 2017, 20(2): 83–91. doi: 10.1016/j.mattod.2016.10.004

[19] Chakraborty, B., Matte, H.S.S.R., Sood, A.K., Rao, C.N.R., Layer-dependent resonant Raman scattering of a few layer MoS_2, J. Raman Spectrosc., 2013, 44(1): 92–96. doi: 10.1002/jrs.4147

[20] Li, H., Zhang, Q., Yap, C.C.R., Tay, B.K., Edwin, T.H.T., Olivier, A., et al., From bulk to monolayer MoS_2: evolution of Raman scattering, Adv. Funct. Mater., 2012, 22(7): 1385–1390. doi: 10.1002/adfm.201102111

[21] Yao, Y., Ao, K., Lv, P., Wei, Q., MoS_2 coexisting in 1T and 2H phases synthesized by common hydrothermal method for hydrogen evolution reaction, Nanomaterials (Basel), 2019, 9(6): 844. doi: 10.3390/nano9060844

[22] Venkateshwaran, S., Senthil Kumar, S.M., Provoking metallic 1T phase conversion of 2H-MoS_2 via an effectual solvothermal route for electrocatalytic water reduction in acid, ACS Sustain. Chem. Eng., 2022, 10(16): 5258–5267. doi: 10.1021/acssuschemeng.2c00381

[23] Saadati, M., Akhavan, O., Fazli, H., Single-layer MoS_2–MoO_{3-x} heterojunction nanosheets with simultaneous photoluminescence and co-photocatalytic features, Catalysts, 2021, 11(12): 1445. doi: 10.3390/catal11121445

[24] Geng, X., Sun, W., Wu, W., Chen, B., Al-Hilo, A., Benamara, M., et al., Pure and stable metallic phase molybdenum disulfide nanosheets for hydrogen evolution reaction, Nat. Commun., 2016, 7: 10672. doi: 10.1038/ncomms10672

[25] Kothaplamoottil Sivan, S., Padinjareveetil, A.K.K., Padil, V.V.T., Pilankatta, R., George, B., Senan, C., et al., Greener assembling of MoO_3 nanoparticles supported on gum arabic: cytotoxic effects and catalytic efficacy towards reduction of p-nitrophenol, Clean Technol. Environ. Policy, 2019, 21(8): 1549–1561. doi: 10.1007/s10098-019-01726-9

[26] Sharma, R.K., Reddy, G.B.S., Synthesis and characterization of α-MoO_3 microspheres packed with nanoflakes, J. Phys. Appl. Phys., 2014, 47(6): 065305. doi: 10.1088/0022-3727/47/6/065305

[27] Manikandan, R., Raina, G., Hydrothermally synthesized 2H-MoS_2 under optimized conditions – a structure and morphology analysis, Phys. Scr., 2022, 97(12): 125808. doi: 10.1088/1402-4896/ac9d6f

[28] Rui, S., Li, Z., Meng, L., Wang, Q., Xu, J., Zhao, Y., et al., Citric acid and plasma treated MoS_2 for high-performance supercapacitors, J. Mater. Chem. C, 2025, 13(2): 849–857. doi: 10.1039/D4TC04432K

[29] Mannayil, J., Pitkänen, O., Mannerkorpi, M., Kordas, K., Optimization and scalability assessment of supercapacitor electrodes based on hydrothermally grown MoS_2 on carbon cloth, Nanoscale Adv., 2024, 6(18): 4647–4656. doi: 10.1039/D4NA00368C

[30] Yuan, X., Xu, J., Zhao, Y., Rui, S., Wang, Q., Meng, L., et al., Plasma treatment of bismuth-doped MoS_2 with excellent supercapacitor performance, J. Mater. Chem. C, 2025, 13(16): 8179–8187. doi: 10.1039/D5TC00767D

[31] Al-Abawi, B.T., Parveen, N., Ansari, S.A., Controllable synthesis of sphere-shaped interconnected interlinked binder-free nickel sulfide@nickel foam for high-performance supercapacitor applications, Sci. Rep., 2022, 12(1): 14413. doi: 10.1038/s41598-022-18728-1

[32] Ansari, M.Z., Seo, K.-M., Kim, S.-H., Ansari, S.A., Critical aspects of various techniques for synthesizing metal oxides and fabricating their composite-based supercapacitor electrodes: a review, Nanomaterials, 2022, 12(11): 1873. doi: 10.3390/nano12111873

[33] Parveen, N., Ansari, M.O., Ansari, S.A., Kumar, P., Nanostructured titanium nitride and its composites as high-performance supercapacitor electrode material, Nanomaterials, 2023, 13(1): 105. doi: 10.3390/nano13010105

[34] Parveen, N., Alsulaim, G.M., Alsharif, S.A., Almutairi, H.H., Alali, H.A., et al., Renewable biopolymer-derived carbon–nickel oxide nanocomposite as an emerging electrode material for energy storage applications, J. Sci. Adv. Mater. Devices, 2023, 8(3): 100591. doi: 10.1016/j.jsamd.2023.100591